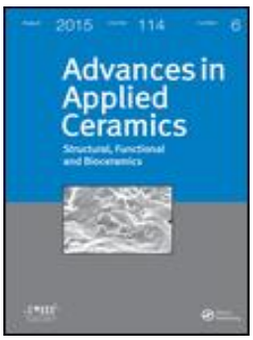

Taylor & Francis
Taylor & Francis Group

Advances in Applied Ceramics

Structural, Functional and Bioceramics

ISSN: 1743-6753 (Print) 1743-6761 (Online) Journal homepage: http://www.tandfonline.com/loi/yaac20

Fracture toughness in some hetero-modulus composite carbides: carbon inclusions and voids

O. Popov & V. Vishnyakov

To cite this article: O. Popov & V. Vishnyakov (2016): Fracture toughness in some hetero-modulus composite carbides: carbon inclusions and voids, Advances in Applied Ceramics, DOI: 10.1080/17436753.2016.1208470

To link to this article: http://dx.doi.org/10.1080/17436753.2016.1208470

Published online: 21 Jul 2016.

Fracture toughness in some hetero-modulus composite carbides: carbon inclusions and voids

O. Popov*[1] and V. Vishnyakov[2]

Structure and mechanical characteristics of dense ceramic composites synthesised by reactive hot pressing of TiC–B_4C powder mixtures at 1800–1950°C under 30 MPa were investigated by X-ray diffraction, scanning electron microscopy and energy dispersive X-ray spectroscopy (SEM and EDX). The results show that during hot pressing solid-phase chemical reaction $2TiC + B_4C = 2TiB_2 + 3C$ has occurred with final products like TiB_2–TiC–C, TiB_2–C or TiB_2–B_4C–C hetero-modulus composite formation with around one micrometer size carbon precipitates. The fracture toughness depends on the amount of graphite precipitation and has a distinct maximum K1C = 10 MPa $m^{1/2}$ at nearly 7 vol.-% of carbon precipitate. The fracture toughness behaviour is explained by the developed model of crack propagation. Within the model, it is shown that pores (voids) and low-modulus carbon inclusions blunt the cracks and can increase ceramic toughness in some cases.

Keywords: Hetero-modulus ceramics, Carbides, Toughness, Modelling

Introduction

Carbide-based ceramics are known and used for more than 100 years as they possess excellent properties such as high melting temperature, high hardness and high electrical conductivity (see for instance review works edited by Matkovich[1] and references within.). Exceptional properties make it possible to use them as structural materials under extreme conditions, at ultrahigh temperatures[2–4] and as a lightweight armour.[5] However, the main issue for all materials based on covalently bond structures is their brittleness. Classic way to enhance ceramic fracture resistance, e.g. toughness, is by building layered systems, for instance, adding metals[6] or other materials.[7] In the case of combination with metals or polymers the material heat resistance decreases significantly. Composites containing purely refractory phases do not possess such flow. In this case the toughening mechanisms can be classified under three main groups.[8] First in an intrinsic fracture toughness enhancement based on frontal process zone expansion which increases the fracture energy consumed in the damaged zone ahead of a crack tip. This includes microcracking due to localised internal stresses around the second phase inclusions[9] as well as so called transformation toughening.[8] To second group belong cases when extrinsic fracture toughness enhancement is provided by means of crack surface bridging with second phase, for instance fibers[10] or high aspect ratio grains.[11] The third group contains materials with the crack deflection mechanisms.[8,11]

Lately the new way of brittle material toughening was developed for so called hetero-modulus ceramics (HMC). It is provided by combination of high Young's modulus (400–700 GPa) matrix with low Young's modulus (15–50 GPa) graphite or graphite-like boron nitride inclusions.[12–14] An additional advantage of HMC, as is mentioned in Shabalin *et al.*,[15] is their machinability with the conventional tools. Low-modulus phases of graphite and hexagonal boron nitride are not tough materials on their own account.[16] Thus, the improvement of super hard ceramic mechanical characteristics with those phase addition should be explained with the interphase structure phenomena. In some respect a soft inclusion works in the same manner as an empty void e.g. pore.

It is well known that an increase in porosity leads to a dramatic strength decrease in most cases. For instance, Bris *et al.*[17] showed the effect in steels while Samborski and Sadowski[18] observed the same for alumina and magnesia. Li and Aubertin[19] summarised similar results for a wide range of non-metal materials. However, there are other works[20,21] claiming that in some cases porosity can have a negligible effect on the fracture energy and toughness or even positively influence mechanical properties.[20,22] It is worth mentioning that Rice[20] presented results for alumina fracture toughness improvement with small (up to 15 vol.-%) amount of ~1 μm pores and rather similar data were obtained for porous MgO. Gnesin[22] has also mentioned the possibility of alumina

[1]Faculty of Physics, Taras Shevchenko National University of Kiev, 4 Hlushkov Ave., Kiev 03187, Ukraine
[2]Materials Research Institute, University of Huddersfield, Huddersfield, HD1 3DH, UK

*Corresponding author, email alexey.popov1861@gmail.com

Published by Taylor & Francis on behalf of the Institute
Received 6 March 2016; accepted 27 June 2016
DOI 10.1080/17436753.2016.1208470

fracture toughness increasing by the little 'intergranular' pores.

Theoretical analysis of crack front – void interaction was mentioned earlier by Broek[23] who considered the possibility of crack capture in a metal plate by the round hole and presented experimental investigation of such capture in aluminium-based alloys. However it was also shown that all the beneficial effects are being downturned by the weakening of the material between the hole and a crack and by the increase of the crack length as soon as the void became a part of the total defect.

One of the early works[24] has evaluated porous ceramic fracture toughness where spherical pores were shown as being able to improve matrix mechanical characteristics by blunting of the crack tip. Unfortunately, the authors did not take into account a case of the pores affecting the crack front (the case was later analysed in Martin[25]). The developed model predictions were experimentally confirmed with limited types of ceramic foams only. Yoshida *et al.*[26] evaluated fracture energy of porous alumina by accounting the crack branching and demonstrated by the experiments the positive effect of pores on the material fracture energy. It should be noted though that the model was only applicable to the high-porosity (>35%) materials which mechanical characteristics were not claimed being higher than that of the dense material.

In summary, although there is some theoretical and practical understanding of porosity influence upon ceramic toughness[21,23,24,26] there is still no universal explanation for all experimental results.[18,20] The existing models do not explain the behaviour of porous alumina and can hardly be used to explain the observed ceramic matrix reinforcement with low-modulus inclusions. Hence, the correct description of crack – void interaction in brittle materials as well as the link between fracture toughness and the strength of ceramics remains as an unresolved problem.

As has been shown previously,[27] sintering of 2TiC–B_4C powder at 2100°C leads to TiB_2 phase creation, with extra carbon segregated as graphite inclusions in diboride matrix. Such inclusions are emerging as a result of chemical reaction; they are almost spherical and thus ideal objects for an investigation.

The paper presents an investigation of the almost spherical low-modulus inclusion influence on fracture toughness of reactive hot-pressed TiC–TiB_2–B_4C–C HMC and demonstrates, with developed crack propagation model how 'soft' inclusions can toughen ceramics.

Experimental

Commercially available powders of TiC (30–50 μm) and B_4C (60 μm) (all of them produced by Donetsk Reactive Factory, Ukraine) were used as starting materials. The material purity was 99.00 at.-%. The powder mixtures of different compositions (Table 1) were grinded in a planetary mill for 15 minutes and hot-pressed in a graphite die. Synthesis temperature ranged from 1800 to 1950°C and was chosen an optimum one for the dense ceramic creation. The applied pressure of 30 MPa and isothermal dwelling time of 16 min were used for hot-pressing procedure.

The bulk densities of obtained materials were measured using the Archimedes method and the crystalline phases in the sintered specimens were determined by X-ray diffractometry (XRD) (DRON–4M, St. Petersburg, Russia). Microstructural observations and local compositional analysis measurements were taken with scanning electron microscopy and energy dispersive X-ray spectroscopy (SEM and EDX) (Carl Zeiss, Germany and EDAX, USA). For further investigation, some specimen surfaces were polished with diamond abrasive media. Hardness HV measurements with a Vickers indenter were performed with two different loads of 4.9 N and 147 N for 20 s holding time on the polished surfaces. Fracture toughness was estimated by measuring the crack lengths generated by Vickers indenter with a load of 147 N.[28] The heat effect and adiabatic temperature were calculated using thermochemistry data from the NIST Chemistry WebBook.[29]

Table 1 Initial powder composition and sintering temperature

Sample number	TiC, at.-%	B_4C, at.-%	Sintering temperature, °C
1	4.3	95.7	1900
2	7.4	92.6	1850
3	13.8	86.2	1800
4	21	79	1800
5	28.5	71.5	1800
6	44.4	55.6	1800
7	61.5	48.5	1850
8	76.2	23.8	1900
9	86.5	13.5	1900
10	93.2	6.8	1950

Results and discussion

The XRD spectra of hot-pressed ceramics are presented in Fig. 1. It is evident that the sintering process causes chemical reaction between TiC and B_4C components with production of TiB_2 and graphite formation. This process can be described, in line with,[27] by the following chemical reaction:

$$2TiC + B_4C = 2TiB_2 + 3C. \quad (1)$$

On the above basis, the sintered materials have compositions, shown in Table 2.

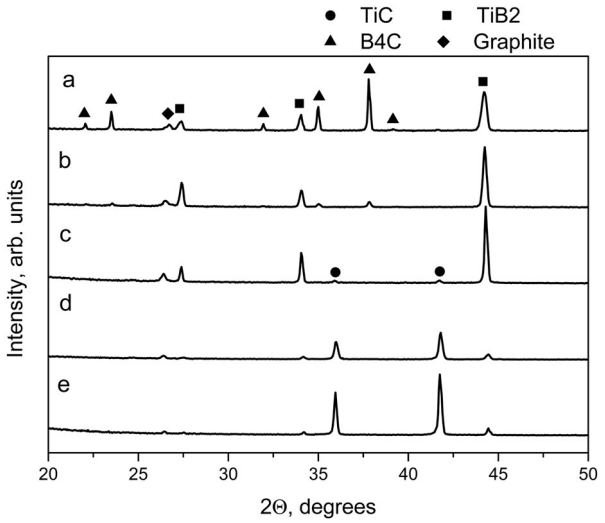

1 XRD spectra of sintered samples

Table 2 Composition* and density of the samples after hot pressing

Number	TiC, vol.-%	B_4C, vol.-%	TiB_2, vol.-%	C, vol.-%	ρ, g cm^{-3}
1	0	89.7	6.8	3.5	2.64
2	0	82.2	11.8	6	2.79
3	0	67.3	21.6	11.1	3.12
4	0	50.7	32.6	16.7	3.4
5	0	33.9	43.7	22.4	3.64
6	1	0	65	34	4.15
7	34.5	0	43.3	22.2	4.41
8	61.2	0	25.6	13.2	4.72
9	78.7	0	14.1	7.2	4.83
10	89.4	0	7	3.6	4.79

*Content of different phases was estimated basing on the initial powder compositions and considering reaction (1) occurring during the sintering process.

Typical structure of cleaved (not polished) stoichiometric composite (sample number 6, Tables 1 and 2) is shown on Fig. 2. It should be noted that the presented images were taken by the backscatter detector in composition mode; this implies that the level of grey is roughly proportional to the average Z at the imaging point, for instance carbon inclusions will appear almost black. The first image (Fig. 2) can be described as from the material constructed of large grey appearing grains (1) alternated with non-uniform mixture based on some darker appearing phase (2). The large areas of bright submicron particles (3) as well as many of darker spherical inclusions with sizes between 0.5 and 3 μm (4) should be also noted. Considering XRD results (Fig. 1) the areas (1) should be titanium diboride, areas (2) – mixture of carbon and titanium diboride, (4) could be carbon inclusions and white particles – titanium carbide remnants.

The distribution of C and Ti atoms in a polished sample 8 section was investigated with EDX (Fig. 3) and XRD analysis (Table 2) proved light grey and grey areas to be TiC and TiB_2 as well as black ones to be the graphite inclusions. Typical ultrathin eutectic structure of TiC–TiB_2 matrix is also presented in Fig. 3. TiC content in the initial powder increasing produces further composite structure changes, as is shown in Fig. 4*b* where TiC-based matrix with distributed

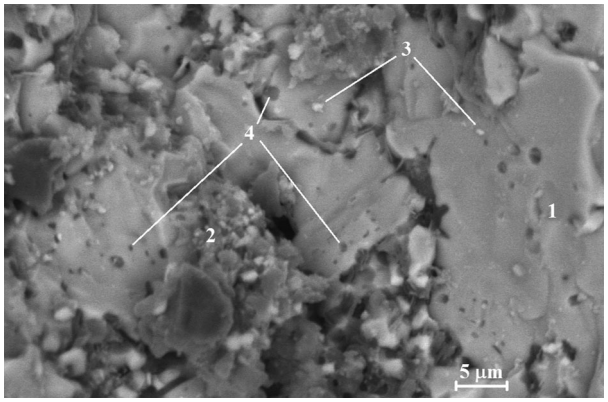

2 SEM micrograph (fracture surface, sample 6, backscattered electrons): 1 – TiB_2 grains, 2 – C-TiB_2 mixture, 3 – TiC remnants, 4 – graphite clusters

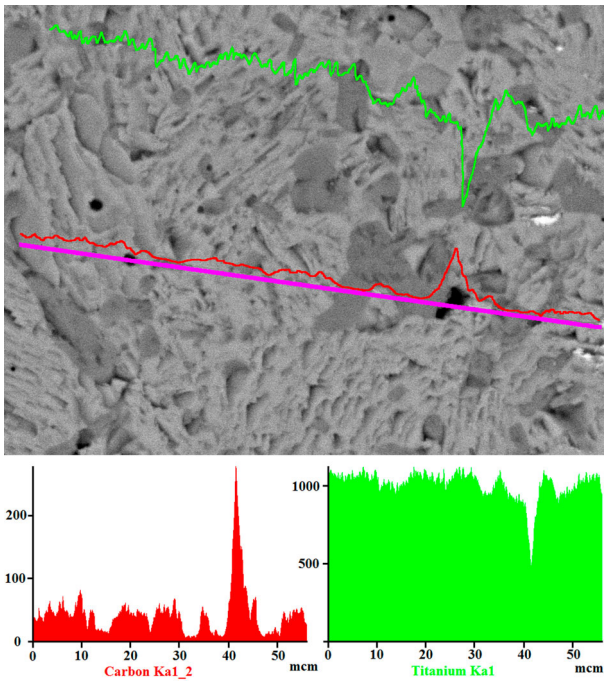

3 SEM backscatter image and EDX line profiles (polished section, sample 8)

carbon inclusions is presented. As it could be expected, samples 1–5 with greater boron carbide amount have similar structure with B_4C–TiB_2 matrix and carbon inclusions (Fig. 4*a*).

It should be noted that most of the composites were fully densified at temperatures not more than 1850°C during 16 minutes while as is shown in Wang *et al.*[2] titanium diboride can be densified at similar conditions during 60 minutes and TiC–C composites were densified by Shabalin *et al.*[12] at temperatures more than 2200°C. Charge shrinkage in presented case can be intensified because of new phase formation during the hot pressing. Reaction (1) heat effect increases almost linearly with temperature from $\Delta H \approx -170$ kJ mole^{-1} at 1000°C to $\Delta H \approx -220$ kJ mole^{-1} at 1800°C.[29] Besides, boron carbide formation enthalpy turns positive at 1000°C thus, B_4C phase becomes metastable at higher temperatures, and may begin to decompose in contact with TiC grains. Boron atoms diffuse into titanium carbide displacing carbon and forming TiB_2 clusters. Carbon atoms remaining after boron carbide decomposition, as well as those of having been displaced form graphite interlayer between B_4C and newly appearing TiB_2 particles. Similar interlayer can appear between TiC and TiB_2 as well. These soft graphite areas emerging under external pressure provoke intergranular slips and lead to the charge consolidation. It should be also noted that 16-minute densification temperature values (minimum hot-pressing temperature at which maximum possible density can be achieved during 16 minutes) are lower (1800°C) near the middle of composition interval (samples 3–6, Tables 1 and 2) where reaction mass content is higher. Latter proved that the densification process of sintered materials depends strongly on the reaction (1).

Sintered material microhardness/composition dependence (Fig. 5*a*) has a minimum for stoichiometric sample

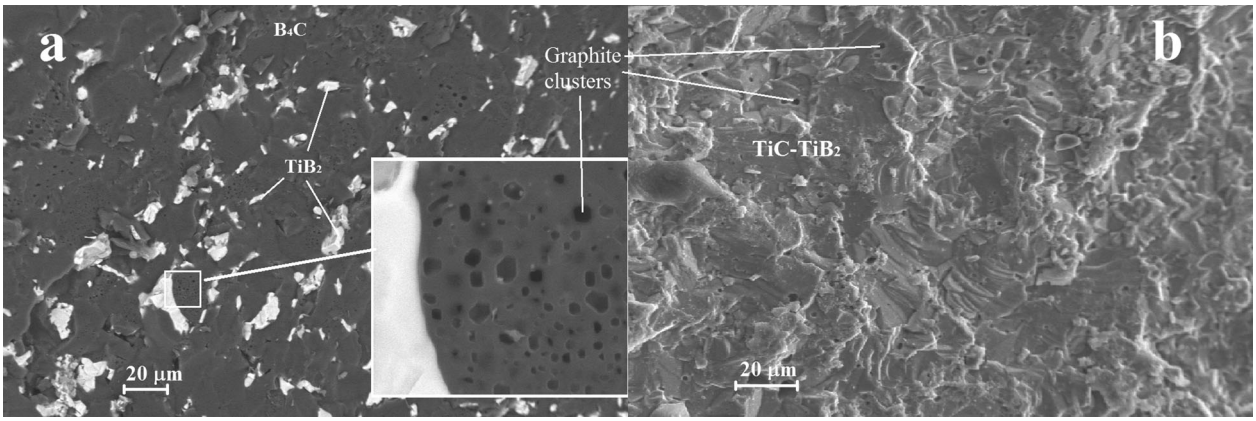

4 SEM micrographs (fracture surfaces, backscattered electron image): *a* – sample 1, *b* – sample 9

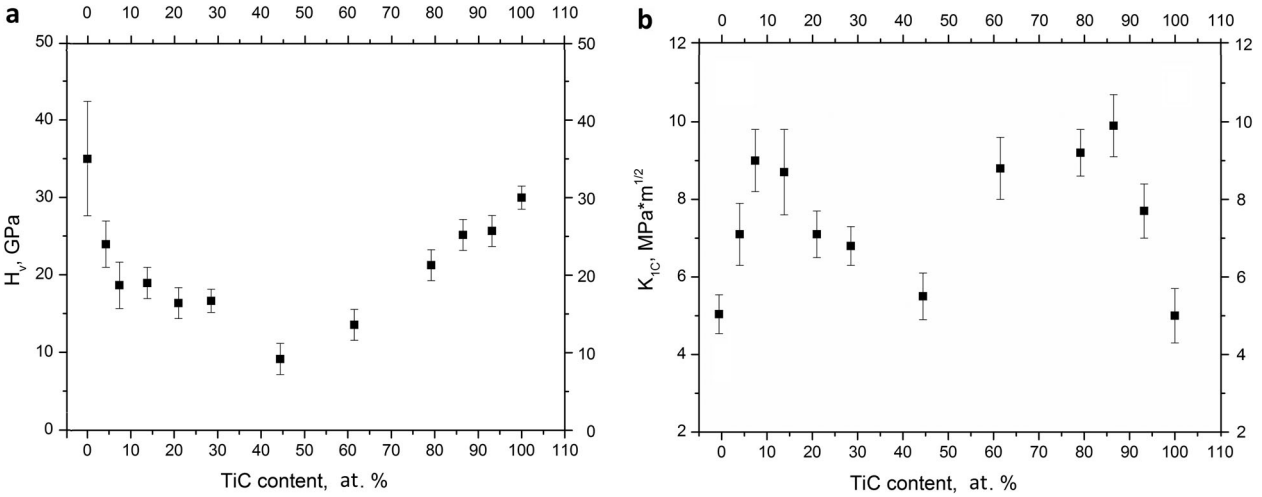

5 Sintered composite hardness *a* and fracture toughness *b*. Mechanical properties of boron and titanium carbides (data for points at TiC concentration 0 and 100 at.-%) are in accordance with[14,15,31,32]

6. In general, the hardness is lower than observed in a similar ceramics created by the laser processing.[30] The same minimum can be seen in a corresponding fracture toughness curve though alongside with two distinct maximums (Fig. 5*b*). It should be noted (Table 3) that the maximums are in the same graphite content. It is clear that sintered material fracture toughness depends not on the type of matrix but predominately on carbon inclusion content. So, as it was shown in,[15] graphite being low-modulus phase should block cracks in the material.

Table 3 Mechanical properties of sintered ceramics

Sample number	Matrix	C, vol.-%	HV15, GPa	K_{1C}, MPa·m$^{1/2}$	HV0.5, GPa
1	B_4C–	3.5	18.3	7.1	24
2	TiB_2	6	19	9.0	18.7
3		11.1	19.6	8.7	19
4		16.7	11.4	7.1	16.4
5		22.4	12	6.8	16.7
6	TiB_2	34	4.3	5.5	9.2
7	TiC–	22.2	10.8	8.8	13.6
8	TiB_2	13.2	13.8	9.2	21.3
9		7.2	19.4	9.9	25.2
10		3.6	19.3	7.7	25.7

Theoretical description

To confirm the possibility of a ceramic material strengthening with the carbon clusters (inclusions) a model for porous material fracture toughness estimation has been developed. The model is based on the experimental fact of crack front bending between reinforcing particles[25] before final destruction of the material. In,[25] matrix strengthening was connected with a crack front critical linear strain T_C (the crack front elastic energy per length unit which should be accumulated for crack propagation) and elastic energy increasing because of front bending, but neither T_C value nor reinforcing particle destruction conditions were represented.

Let us consider a loaded crack with stress intensity coefficient K_1 in a brittle material. The expression for linear strain T can be obtained with integration of elastic energy density considering Irvine relations[33] for stress distribution near the crack tip:

$$T = \frac{1}{2E}\iint_{0,\,r_0}^{2\pi,D}\left(\frac{K_1}{\sqrt{2\pi r}}f(\psi)\right)^2 dV = \alpha\frac{K_1^2}{E}(D-r_0), \quad (2)$$

where $\alpha = 9/16$ – coefficient obtained with $f(\psi)$

integration, r_0 – crack tip radius estimated as

$$r_0 = \frac{100}{2\pi}\left(\frac{K_{1C}}{E}\right)^2, \tag{3}$$

considering that the material before a crack tip will be destroyed when the stress reaches 0.1E.[34] In equations (2) and (3) E and K_{1C} mean Young's modulus and fracture toughness respectively. It is well known that Irvine relations are approximate and can be used only for the material near a crack front. On the other hand a force applied to the crack area (σ_0S) must be compensated with additional stresses in the material. Calculation shows that the distance in which Irvin stresses compensate all the force is $C/2$ ($2C$ is the crack length). So D parameter in (2) should be estimated as $C/2$ and, considering $r_0 << C/2$ expression (2) transforms into:

$$T = \frac{\alpha C K_1^2}{2E} \tag{4}$$

Then the critical linear strain T_{C0} can be estimated as

$$T_{C0} = \frac{\alpha C K_{1C}^2}{2E} = \alpha\frac{C}{2}\gamma_0. \tag{5}$$

Here

$$\gamma_0 = \frac{K_{1C}^2}{2E} \tag{6}$$

is the material fracture energy.[35]

Now we can consider uniqueness of crack propagation in a matrix containing inclusions. As it was shown in Martin[25] crack front in such structure is sagging until the particles are crashed. In this case crack propagation work (γ) includes not only energy for material cleavage (γ_0) but also crack front elastic energy increasing:

$$\gamma dS = \gamma_0 dS + T_{C0} dl \Rightarrow \gamma = \gamma_0 + T_{C0}\frac{dl}{dS}, \tag{7}$$

Let the voids be spherical with the average radius R_p and concentration η, evenly distributed in ceramic matrix with fracture energy and Young's modulus γ_0 and E_0 respectively. Reduction of load-carrying intersection of the sample causes fracture energy decreasing:

$$\gamma_1 = \gamma_0(1-\eta). \tag{8}$$

Critical linear strain (5) alters in a similar way:

$$T_{C1} = \alpha C\gamma_1(1-\eta)/2. \tag{9}$$

On the other hand, as is shown in Cherepanov,[36] maximum stress σ in a crack tip with circumferential (R_p) void can be estimated as:

$$\sigma = 3\frac{K_1}{\sqrt{2\pi R_p}}. \tag{10}$$

Thus the void leads to the significant decreasing of stress concentration, so linear strain is reduced to

$$T_p = T\frac{9r_0}{R_p}, \tag{11}$$

where r_0 is a crack tip radius (3). Considering that the material in a caved crack tip will be cleaved when $\sigma =$ 0.1E, the expression for critical stress intensity coefficient for such crack front area can be obtained based on equation (10):

$$K_{1Cp} = \frac{\sqrt{2\pi R_p}E}{30}, \tag{12}$$

and the corresponding fracture energy (6) should be:

$$\gamma_p = \frac{\pi R_p E}{450}. \tag{13}$$

Hence, if $R_p > r_0$ a spherical pore can not only weaken the material, but also detain crack in it with effectiveness increasing with the pore radius.

Such confinement is shown in Martin[25] as leading to crack front sagging in a way presented in Fig. 6 which causes matrix destruction energy increasing (7) with the elongation

$$\frac{dl_1}{dS} = \frac{1}{R_1} \tag{14}$$

Thus matrix fracture energy is

$$\gamma_m = \gamma_1 + \frac{1}{R_1}T_{C1} = \gamma_0\left(1 + \frac{\alpha C(1-\eta)}{2R_1}\right)(1-\eta). \tag{15}$$

Here R_1 is the crack front curvature (see Fig. 7) which can be calculated as

$$R_1 = \frac{L_1}{2\sin(\theta)} = \frac{L - 2R_p\cos(\varphi)}{2\sin(\theta)}, \tag{16}$$

$$L_1 = L - L_2, \tag{17}$$

$$L_2 = 2R_p\cos(\varphi), \tag{18}$$

$$L = \sqrt[3]{\frac{4\pi R_p^3}{3\eta}}, \tag{19}$$

where L is an average distance between pores. Brief analysis of (15) shows that matrix fracture energy with a straight front crack ($\phi = \theta = 0$; $R_1 \to \infty$) reduces to γ_1 (8) and begins increasing significantly when front curvature radius R_1 becomes comparable to a crack length C.

So now we have expressions to estimate effective fracture energies of 'pore' (13) and matrix (15) based on matrix and porosity properties as well as on crack front bending parameters (ϕ and θ). The latter will change during front bending process reaching their critical values ϕ_c and θ_c when over-pore material will at last be crashed.

To find the critical crack front curvature parameters we should consider that the crack sagging leads to stress redistribution between incurved and domed areas (see l_1 and l_2, Fig. 7). For the crack propagation in incurved area there should be accumulated critical linear strain T_{C1} (9). Linear strain unit is N, so it is natural to suppose domed/incurved area interaction to be force-like. The similar approach for dislocation movement was developed in Foreman and Makin.[37] So, taking (11) into account, we can write the expression for linear strain (T_2) in l_2 area (Fig. 7):

$$T_2 = 9T_{C1}(1 + 2\sin\theta)r_0/R_p. \tag{20}$$

In principle the crack could grow in a way shown in Fig. 6 until T_2 reaches T_{C1} crashing over-pore material.

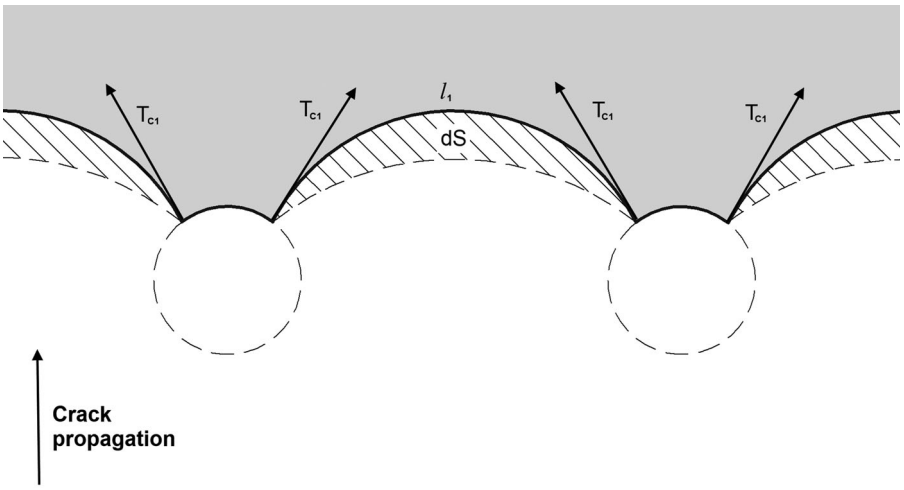

6 The crack front is sagging between two spherical pores

But such crack front bending leads to R_1 decreasing (16) hence causes increasing of matrix effective fracture energy (15) and at some R_1 value Fig. 6 ceases representing the most energy-optimal way of crack propagation. In this case, concaved (l_1) front area begins to move as it is shown in Fig. 8, when simultaneously with l_1 lengthening l_2 shortening occurs resulting in φ increasing. This is the way of 'cutting' over-pore material instead of 'crashing' it. Hence formula (7) for the effective crack propagation work goes to:

$$\gamma = \gamma_1 + T_{C1}\frac{dl_1}{dS} + T_2\frac{dl_2}{dS} = \gamma_1 + T_{C1}\frac{dl_1 + hdl_2}{dS}, \quad (21)$$

where, considering (20)

$$h = T_2/T_{C1} = 9(1 + 2\sin\theta)r_0/(R_p(1 + 2r_0/R_p)^2). \quad (22)$$

New (Fig. 8) front elongation value can be estimated as follows:

$$\frac{dl_1 + hdl_2}{dS} = \frac{2\left(1 - h\dfrac{\cos\theta}{\sin\varphi}\right)}{2R_1\sin^2\theta + \dfrac{\cos\theta}{\sin\varphi}(L\cos\varphi - 2r\cos^2\varphi)}. \quad (23)$$

The crack grows in a second (Fig. 8) way when the front propagation energy (7) is more than that of (21) or, considering (14) and (23) the corresponding condition can be presented as

$$\frac{1}{R_1} > \frac{2\left(1 - h\dfrac{\cos\theta}{\sin\varphi}\right)}{2R_1\sin^2\theta + \dfrac{\cos\theta}{\sin\varphi}(L\cos\varphi - 2r\cos^2\varphi)}. \quad (24)$$

Such movement can be described as φ magnification at a constant θ and in fact is front curvature relaxation and

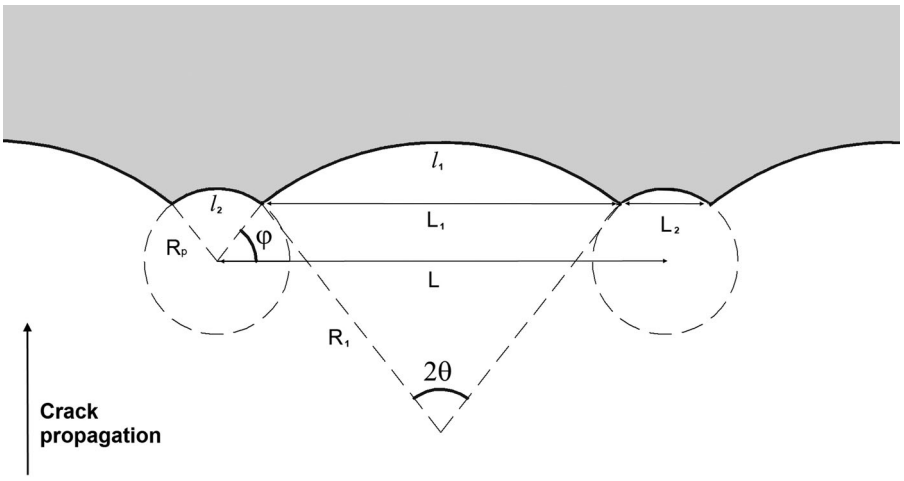

7 Crack front geometrical characteristics

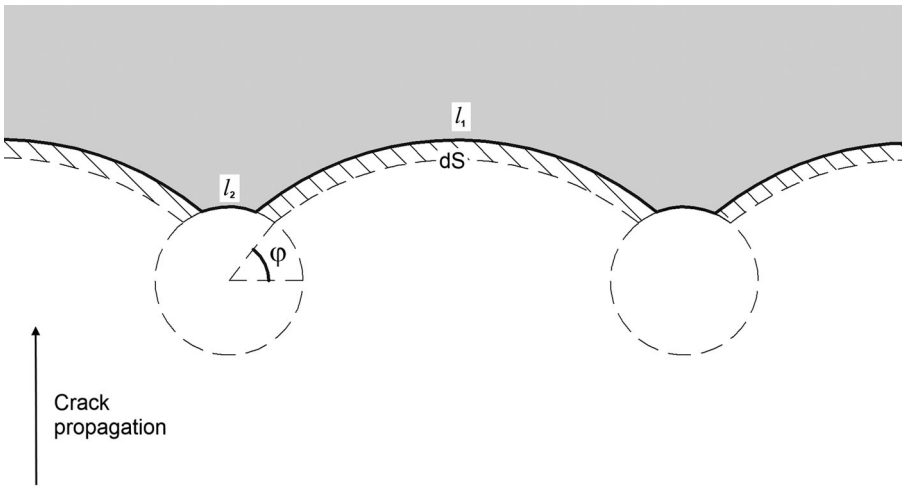

8 The crack front is 'cutting' over-pore material

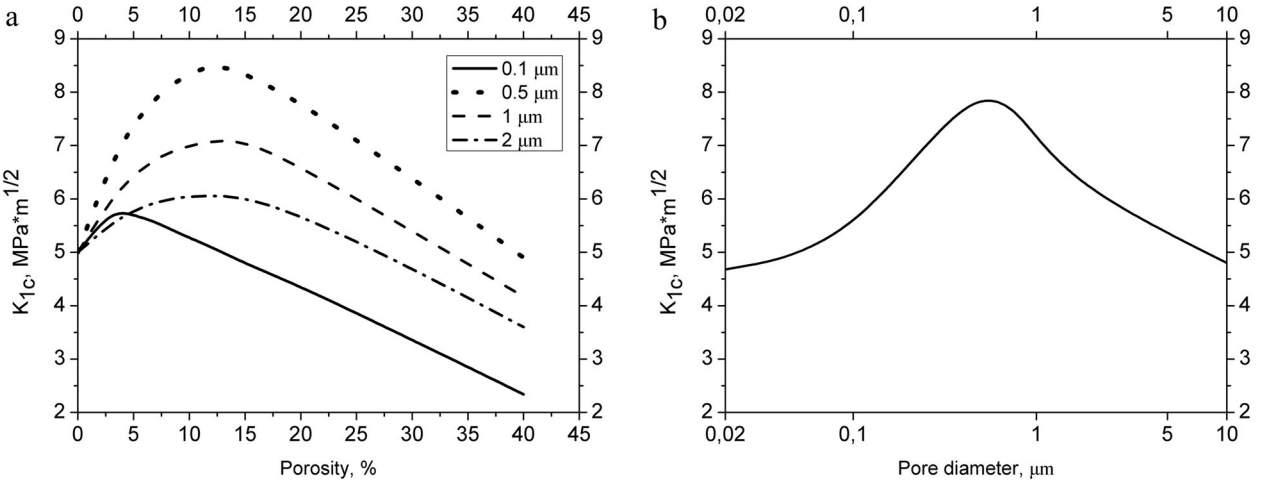

9 Dependence of ceramic fracture toughness on voids concentration with different void diameters *a* and on void diameter at the concentration of 12% *b*

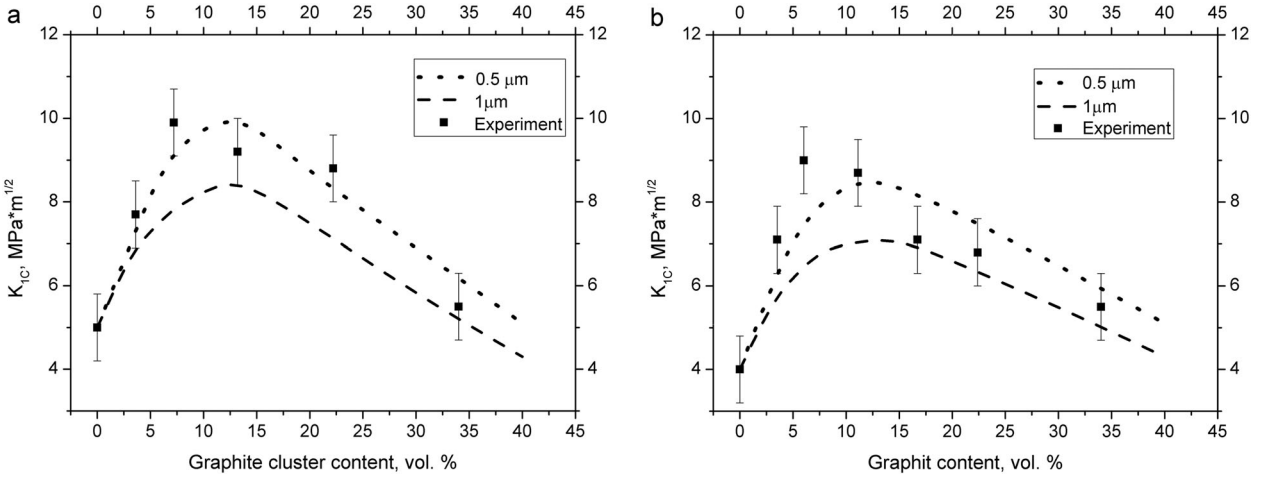

10 Dependence of ceramic fracture toughness on graphite cluster content: *a* – TiC–TiB_2–C (samples 6–10); *b* – B_4C–TiB_2–C (samples 1–6)

logically leads to R_1 increasing (16). Thus at some φ value the condition (24) cannot be fulfilled. Then the crack front once more can propagate in a way presented in Fig. 6 which in its turn can be described as θ magnification at a constant φ. Analysis shows that during the crack growth both ways (Figs. 6 and 8) can occur swapping each other. But this process diminishes l_2 region – the main cause of crack arresting and simultaneously increases T_2 (20) and after reaching critical values of φ_c and θ_c over-pore material should be overcome in a way of crashing

$$T_2 \geq T_{1C} \tag{25}$$

or cutting

$$\varphi \to 90^{\circ}. \tag{26}$$

To estimate these critical parameters we developed an analytical programme which begins with a straight crack front ($\theta = 0$ and $\varphi = 0$). Then step 1 begins with θ increasing while condition (24) checking and when it is fulfilled step 2 begins with φ increasing. When at certain φ value (24) ceases being fulfilled, the front propagation way changes once more and step 1 continues. With this step by step θ and φ magnification critical front curvature φ_c and θ_c values of maximum material fracture resistance can be achieved. Using these parameters one can obtain fracture energy and fracture toughness of ceramic material with spherical pores as follows:

$$\gamma_{ef} = \frac{(L_1\gamma_m + L_2\gamma_p)}{L_1 + L_2}, \tag{27}$$

or, considering (13, 15–19)

$$\gamma_{ef} = \frac{\left(\left(\sqrt[3]{\frac{4\pi}{3\eta}} - 2\cos(\varphi_c)\right)\gamma_0\left(R_p + \frac{\alpha C(1-\eta)\sin(\theta_c)}{\sqrt[3]{\frac{4\pi}{3\eta}} - 2\cos(\varphi_c)}\right)(1-\eta) + \frac{\pi R_p^2 E}{225}\cos(\varphi_c)\right)}{\sqrt[3]{\frac{4\pi}{3\eta}}R_p}$$

and

$$K_{1Cef} = \sqrt{E\gamma_{ef}}, \tag{28}$$

where $E = E_0(1-\eta)^2$ – Young's modulus of porous material.[38]

To analyse material properties vs. void concentration dependences of the ceramic matrix materials we have used mechanical characteristics of a model material. Matrix properties were considered to be the same as those of TiC: E = 500 GPa, K_{1C} = 5 MPa m$^{1/2}$. Fracture toughness on porosity dependences for different pore radii d is presented in Fig. 9*a* and clearly indicates that spherical low-modulus clusters can improve ceramic mechanical characteristics significantly. As it is shown in Fig. 9*b*, there is the optimal pore diameter value which is supposed to be 0.3–1 μm for the investigated matrix. Larger pores are easier to be 'cut' by a crack front while smaller ones are not so efficient in crack tip blunting.

Additional experimental evidence of the conclusion is presented by Jiang *et al.*[14] who have showed that h-BN inclusion influence on B_4C matrix and the effect is dictated by the inclusion size: 10% of submicron BN particles could strengthen the material while 2–3 μm ones just weakened it.

Further calculations were performed considering complex matrix of the investigated materials. Fracture toughness value for TiC–TiB_2 matrix (6.5 MPa m$^{1/2}$; samples 6–10) was used based on published data,[39] and that for B_4C–TiB_2 matrix (5 MPa m$^{1/2}$; samples 1–6) using[40] data. Theoretical curves show fair correspondence to the experimental characteristics of sintered ceramics (Fig. 10). The authors are fully aware that the presented here indentation toughness has its limitations when applied to a porous composite system but here we concentrate mainly on comparative fracture toughness of different compositions rather than on absolute fracture toughness values. On this basis the authors would like to stress the validity of the main statement: low-modulus inclusions and voids (pores) may strengthen ceramic matrix. The exact influence will depend on the ceramic properties but one most likely should have submicron pores to improve fracture toughness.

Conclusions

- A reactive hot-pressing method for TiB_2–TiC–C, TiB_2–C and TiB_2–B_4C–C HMC composite production was developed using B_4C and TiC precursors.
- High-speed densification at relatively low temperatures (not more than 1950°C during 16 minutes) was a result of solid-phase chemical reactions between starting components during the charge consolidation.
- A model for HMC fracture toughness estimation has been developed. The model corresponded to the obtained experimental data and proved that the crack tip blunting in graphite inclusions was the basic cause of sintered composite high properties ($K_{1C} \approx 10$ MPa m$^{1/2}$).

Acknowledgement

The authors acknowledge Prof. I. Shabalin for his helpful suggestions concerning the idea to publish this paper.

ORCiD

O. Popov http://orcid.org/0000-0002-1281-8980
V. Vishnyakov http://orcid.org/0000-0003-3045-3134

References

1. V. I. Matkovich: 'Boron and refractory borides', 1977, Berlin, Springer.
2. W. Wang, Z. Fu, H. Wang and R. Yuan: 'Influence of hot pressing sintering temperature and time on microstructure and mechanical properties of TiB_2 ceramics', *J. Eur. Ceram. Soc.*, 2002, **22**, 1045–1049.
3. R. G. Munro: 'Material properties of titanium diboride', *J. Res. Natl. Inst. Stand*, 2000, **105**, 709–720.
4. R. Köenigshofer, S. Fürnsinn, P. Steinkellner, W. Lengauer, R. Haas, K. Rabitsch and M. Scheerer: 'Solid-state properties of hot-pressed TiB_2 ceramics', *Int. J. Refract. Met. Hard Mater.*, 2005, **23**, 350–357.
5. I. G. Crouch, G. Appleby-Thomas and P. J. Hazell: 'A study of the penetration behaviour of mild-steel-cored ammunition against boron carbide ceramic armours', *Int. J. Impact Eng.*, 2015, **80**, (0), 203–211.

6. G. Wen, S. B. Li, B. S. Zhang and Z. X. Guo: 'Reaction synthesis of TiB–TiC composites with enhanced toughness', *Actamater*, 2001, **49**, 1463–1470.
7. Q. H. Qin: '1 – Introduction to the composite and its toughening mechanisms', in 'Toughening mechanisms in composite materials', (ed. Q. Q. Ye), 1–32; 2015, Cambridge, Woodhead Publishing.
8. H. Awaji, T. Matsunaga and S.-M. Choi: 'Relation between strength, fracture toughness, and critical frontal process zone size in ceramics', *Mater. Trans.*, 2006, **47**, (6), 1532–1539.
9. H. Awaji, S.-M. Choi and E. Yagi: 'Mechanisms of toughening and strengthening in ceramic-based nanocomposites', *Mech. Mater.*, 2002, **34**, 411–422.
10. J. Rödel: 'Interaction between crack deflection and crack bridging', *J. Eur. Ceram. Soc.*, 1992, **10**, 143–150.
11. R. W. Steinbrech: 'Toughening mechanisms for ceramic materials', *J. Eur. Ceram. Soc.*, 1992, **10**, 131–142.
12. I. L. Shabalin, D. M. Tomkinson and L. I. Shabalin: 'High-temperature hot-pressing of titanium carbide-graphite hetero-modulus ceramics', *J. Eur. Ceram. Soc.*, 2007, **27**, 2171–2181.
13. I. L. Shabalin and D. L. Roach: 'Synthetic resin-bonded transition-metal carbide–carbon hetero-modulus ceramics', *J. Eur. Ceram. Soc.*, 2007, **27**, 3527–3538.
14. T. Jiang, Z. Jin, J. Yang and G. Qiao: 'Mechanical property and *R*-curve behavior of the B_4C/BN ceramics composites', *Mater. Sci. Eng A.*, 2008, **494**, 203–216.
15. I. L. Shabalin, Y. Wang, A. V. Krynkin, O. V. Umnova, V. M. Vishnyakov, L. I. Shabalin and V. K. Churkin: 'Physicomechanical properties of ultrahigh temperature heteromodulus ceramics based on group 4 transition metal carbides', *Adv. Appl. Ceram.*, 2010, **109**, (7), 405–415.
16. V. Brožek, V. Dufek, V. Harok and P. Rohan: 'Improvement in boron nitride ceramics prepared by electroconsolidation', *Ceram. Silikáty*, 2003, **47**, 135–140.
17. J. Bris, F. Benítez, A. Mateo, J. Calero, M. Anglada and L. Llanes: 'Fracture toughness of high-density sintered steels', *Anales de Mecánica de la Fractura*, 2006, **2**, 397–401.
18. S. Samborski and T. Sadowski: 'Dynamic fracture toughness of porous ceramics', *J. Am. Ceram. Soc.*, 2010, **93**, (11), 3607–3609.
19. L. Li and M. Aubertin: 'A general relationship between porosity and uniaxial strength of engineering materials', *Can. J. Civ. Eng.*, 2003, **30**, 644–658.
20. R. Rice: 'Grain size and porosity dependence of ceramic fracture energy and toughness at 22°C', *J. Mater. Sci.*, 1996, **31**, 1969–1983.
21. R. Gasirov: 'Porous composite fracture toughness prediction', in 'Models of deformation and destruction of composite materials', (ed. V. Moshev and A. Tashkinov), 41–42; 1988, Sverdlovsk, Ufa Sci. Centre of USSR Ac. of Sci. (in Russian).
22. G. Gnesin: 'Ceramic tool materials', 188; 1991, Kiev, Naukova dumka (in Russian).
23. D. Broek: 'Elementary engineering fracture mechanics', 469; 1982, London, Springer Netherlands.
24. A. F. Schurov, A. M. Shiryaev and A. M. Kotkis: 'Fracture toughness of brittle materials', *Appl. probl. strength. plast.*, 1981, **17**, 108–113 (in Russian).
25. R. H. Martin: 'Composite materials: Fatigue and fracture', Vol. 5, 1995, Philadelphia: American Society for Testing & Materials.
26. K. Yoshida, H. Tsukidate, A. Murakami and H. Miyata: 'Influence of pore size on fracture strength of porous ceramics', *J. Solid Mech. Mater. Eng.*, 2008, **2**, (8), 1060–1069.
27. I. Kazo and A. Popov: 'Mechanical properties of TiB_2–TiC–C* ceramic materials', *Func. Mater.*, 2003, **3**, 503–506.
28. A. G. Evans and E. A. Charles: 'Fracture toughness determinations by indentation', *J. Am. Ceram. Soc.*, 1976, **59**, 371–372.
29. NIST Chemistry WebBook: http://webbook.nist.gov/chemistry/03/05/2013.
30. R. M. White and E. C. Dickey: 'Mechanical properties and deformation mechanisms of B_4C–TiB_2 eutectic composites', *J. Eur. Ceram. Soc.*, 2014, **34**, (9), 2043–2050.
31. A. A. El Mel, E. Gautron, F. Christien, B. Angleraud, A. Granier, P. Souček, P. Vašina, V. Buršíková, M. Takashima, N. Ohtake, H. Akasaka, T. Suzuki and P. Y. Tessier: 'Titanium carbide/carbon nanocomposite hard coatings: a comparative study between various chemical analysis tools', *Surf. Coat. Technol.*, 2014, **256**, 41–46.
32. L. Vargas-Gonzalez, R. F. Speyer and J. Campbell: 'Flexural strength, fracture toughness, and hardness of silicon carbide and boron carbide armor ceramics', *Int. J. Appl. Ceram. Technol.*, 2010, **7**, (5), 643–651.
33. H. Tada, P. C. Paris and G. R. Irwin: 'The stress analysis of cracks handbook', 3rd edn, 2000, New York, American Society of Mechanical Engineers.
34. G. M. Bartenev and Yu. S. Zuyev: 'Strength and failure of visco-elastic materials', 1968, Oxford, Pergamon Press.
35. A. A. Griffith: 'The phenomena of rupture and flow in solids', *Philos. Trans. R. Soc. Lond. A.*, 1920, **A221**, 163–198.
36. G. P. Cherepanov: 'Mechanics of brittle fracture', 1979, New York, McGraw-Hill.
37. A. J. E. Foreman and M. J. Makin: 'Dislocation movement through random arrays of obstacles', *Philos. Mag.*, 1966, **14**, 911–924.
38. A. P. Roberts and E. J. Garboczi: 'Elastic properties of model porous ceramics', *J. Am. Ceram. Soc.*, 2000, **83**, (12), 3041–3048.
39. I. Gotman, N. A. Travitzky and E. Y. Gutmanas: 'Dense in-situ TiB_2/TiN and TiB_2/TiC ceramic-matrix composites: reactive synthesis and properties', *Mater. Sci. Eng. A*, 1998, **244**, (1), 127–137.
40. H. Itoh, K. Sugiura and H. Iwahara: 'Preparation of TiB_2–B_4C composites by high pressure sintering', *J. Alloy. Compd.*, 1996, **232**, 186–191.